Chemical Synthesis

Research Article

SrSnO₃ perovskite *vs.* Nd₂Sn₂O₇ pyrochlores for oxidative coupling of methane: deciphering the reactive sites difference

Rumeng Ouyang[1,#], Junwei Xu[1,2,#,*], Xusheng Zhong[1], Ying Gong[1], Yameng Liu[1], Xiuzhong Fang[1], Jiating Shen[1], Xiang Wang[1,*] (iD)

[1]Key Laboratory of Jiangxi Province for Environment and Energy Catalysis, College of Chemistry and Chemical Engineering, Nanchang University, Nanchang 330031, Jiangxi, China.
[2]Department of Applied Chemistry, Jiang Xi Academy of Sciences, Nanchang 330096, Jiangxi, China.
[#]Authors contributed equally.

[*]**Correspondence to:** Prof. Xiang Wang, Dr. Junwei Xu, Key Laboratory of Jiangxi Province for Environment and Energy Catalysis, College of Chemistry and Chemical Engineering, Nanchang University, 999 Xuefu Avenue, Nanchang 330031, Jiangxi, China. E-mail: xwang23@ncu.edu.cn; Xujunwei0102@163.com

Abstract

Herein, SrSnO₃ perovskite and Nd₂Sn₂O₇ pyrochlore with definite structures have been synthesized using a hydrothermal method, and the differences in their reactive sites for the oxidative coupling of methane (OCM) are investigated. The primary products of perovskite and pyrochlore are C₂ hydrocarbons and CO$_x$, respectively. The C₂ selectivity of perovskite is primarily affected by basic sites and chemisorbed oxygen species O₂²⁻. For pyrochlore, the key factors affecting methane conversion and CO$_x$ selectivity are the acidic sites and reactive oxygen species (chemisorbed oxygen species and weakly bonded lattice oxygen). The chemisorbed oxygen species of pyrochlore are directly generated through intrinsic oxygen vacancies, whereas those of perovskite are generated through oxygen vacancies created under high-temperature lattice distortions. The tightness of the stacking between [SnO₆] octahedra is the main factor affecting the acidic sites and oxygen vacancies of the two composite oxides. The stacking of [SnO₆] octahedra in pyrochlore is loose, resulting in a relatively weak Sn–O bond strength. During the OCM reaction, the Sn–O bond is prone to breakage, resulting in abundant acidic sites and oxygen vacancies. Additionally, the influence of basic sites on the amount of chemisorbed oxygen species is more important than that

of oxygen vacancies, which is attributed to the fact that basic sites can stabilize chemisorbed oxygen species on the catalyst surface.

Keywords: Oxidative coupling of methane, definite compounds, perovskite, pyrochlore, comparison of reactive sites

INTRODUCTION

Ethylene is widely used as a chemical intermediate to produce plastics and alpha-olefins, and methane is an abundant and relatively cheap natural resource[1,2]. The oxidative coupling of methane (OCM), a single-step reaction that converts methane to ethylene and ethane, has attracted significant attention in the past four decades[2,3]. Following the pioneering work of Keller and Bhasin, nearly thousands of types of catalysts have been developed for OCM[4], including alkali metal oxide modified alkaline earth metal oxides[5], rare earth metal oxides[6], $Mn/Na_2WO_4/SiO_2$[7,8], and composite oxides such as perovskites and pyrochlores[9,10]. In particular, ABO_3 perovskites and $A_2B_2O_7$ pyrochlores are well known for their stable structures[11]. Their A- and B- site cations are easily replaceable, and thus, their surface acidity and basicity can be regulated. Furthermore, both these catalysts have excellent thermal stability, chemical stability, and oxygen ion mobility. Their phase structure is shown in Scheme 1. Considering that their active sites can meet most requirements for OCM, they are ideal catalysts for understanding the effect of active sites on this reaction[12,13]. ABO_3 perovskites and $A_2B_2O_7$ pyrochlores have the following similarities:
(1) A- and B- site cations have a stoichiometric ratio of 1:1.
(2) The A elements generally represent alkaline earth metal and rare earth metal cations, whereas B denotes transition metal cations that coordinate with six oxygen ions to form $[BO_6]$ octahedra[14-16].
(3) Their fine structures are regulated either by the tolerance factor (t)[17] or ionic radius ratio (r_A/r_B).
(4) The A–O bond is more ionic, and the B–O bond is more covalent[18,19].

ABO_3 perovskites and $A_2B_2O_7$ pyrochlores exhibit the following differences:
(1) A-site cations of perovskite are 12-coordinated, whereas those of pyrochlore are 8-coordinated[20,21].
(2) An ideal ABO_3 perovskite exhibits a cubic structure, and it transforms into triclinic, monoclinic, rhombohedral, orthorhombic, and tetragonal crystal structures primarily due to cation displacement, octahedral distortions, and octahedral tilting that maintain corner-sharing connectivity. These structural deviations cause non-cubic perovskites to undergo phase transitions at high temperatures because they all tend to transition to cubic structures[17,22].
(3) The $A_2B_2O_7$ composite oxide contains four sub-crystalline structures, namely layered perovskite ($r_A/r_B > 1.78$), pyrochlore ($1.46 < r_A/r_B < 1.78$), disorder defect fluorite ($r_A/r_B \approx 1.46$), and rare earth C-type ($r_A/r_B \approx 1.17$)[23,24]. The lattice disorder degree changes from ordered to disordered and then to ordered. Except for the layered perovskite phase structure, the other three sub-crystalline phases are cubic with intrinsic oxygen vacancies.

By comparing the similarities and differences between ABO_3 and $A_2B_2O_7$, we can understand the influence of their surface physicochemical properties on OCM and provide a theoretical basis for designing high-performance OCM catalysts. It has been found that Sn-based alkaline earth metal perovskites exhibit good OCM reaction performance, while Sn-based pyrochlore is commonly used in methane combustion reactions[25,26]. Petit *et al.* have prepared tin-based perovskite $ASnO_3$ (A = Ca, Sr, Ba) for OCM reaction using SnO or $SnCl_4$ as a precursor by sol-gel methods. It has shown that the C_2 hydrocarbon selectivity of perovskites prepared by chlorine containing precursor $SnCl_4$ is significantly higher than that of perovskites prepared by SnO as a precursor. The difference could be attributed to the increase in basicity of the catalyst surface due to the presence of bulk or surface Cl^- species[25]. Yang *et al.* found that the OCM reaction
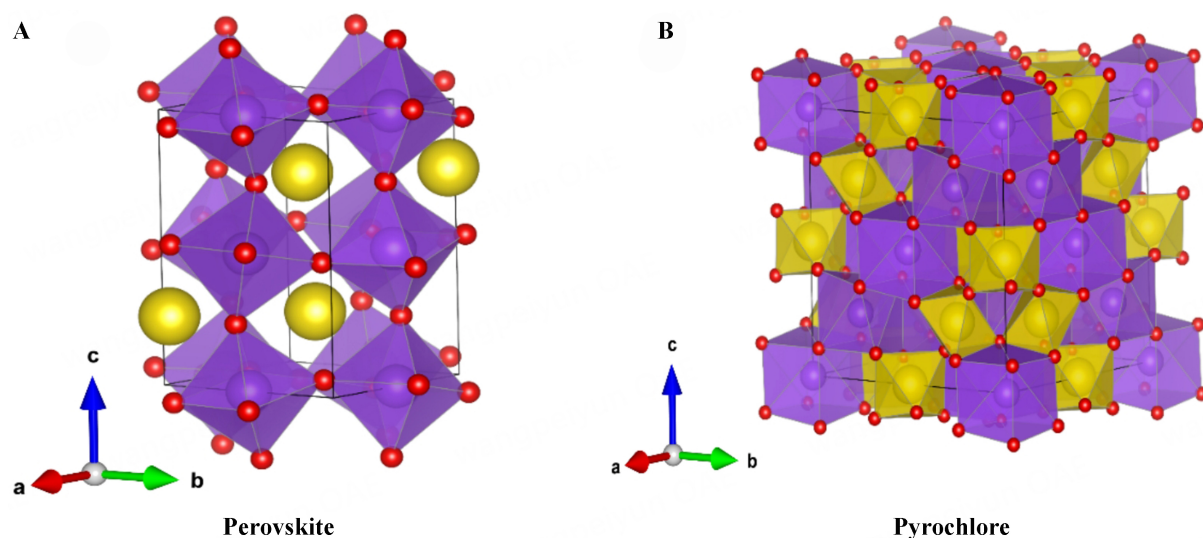
Scheme 1. The phase structures of the (A) perovskite and (B) pyrochlore.

performance of layered perovskites Sr_2TiO_4 and $SrSn_2O_4$ at 1,073 K was higher than that of corresponding $SrTiO_3$ and $SrSnO_3$ perovskites. The increase in methane conversion and C_2 selectivity of layered perovskites is due to the O_2^{2-} species produced by their decomposition under reaction conditions[27]. Park *et al.* synthesized $Ln_2Sn_2O_7$ (Ln = La, Sm, and Gd) pyrochlores using a hydrothermal method for methane combustion reactions. It demonstrated that $La_2Sn_2O_7$ has better catalytic activity than other catalysts. This is due to the lowest Sn–O bond energy in $La_2Sn_2O_7$, which promotes the generation of more surface active sites[26]. Cheng *et al.* synthesized a series of $La_2Co_xSn_{2-x}O_{7-\delta}$ composite oxides with pyrochlore structure by co-precipitation method for methane combustion. They confirmed that with the increase of Co doping content, the strength of the Sn–O bond weakened, which promoted the formation of oxygen vacancies and, thus, benefited the activity of methane combustion[28].

In view of the above research, we are very curious about why tin-based perovskites exhibit OCM reaction activity, while tin-based pyrochlore mainly exhibits methane combustion activity. Comparing the similarities and differences in the crystal structure of the two composite oxides, this study addresses the following questions. How are the acid-base and redox properties of these two complex oxides different, and how do the presence and absence of intrinsic oxygen vacancies affect their oxygen properties? Accordingly, we synthesized two types of composite oxides, namely $ASnO_3$ (A = Ca, Sr, Ba) and $Ln_2Sn_2O_7$ (Ln = La, Pr, Nd), and the two catalysts with the best reaction performance (i.e., $SrSnO_3$ and $Nd_2Sn_2O_7$) were selected for detailed investigation of the variations in their reactive sites. By adopting various characterization techniques, the reasons for the differences in catalytic performance have been revealed, including the distinctions in major products and active sites.

EXPERIMENTAL
Catalyst preparation
$Sr(NO_3)_2$ (99.9%, Aladdin), $Nd(NO_3)_3\cdot6H_2O$ (99.9%, Aladdin), $SnCl_4\cdot5H_2O$ (98.0%, Sinopharm Chemical Reagent Corporation, China), and KOH (99%, Sinopharm Chemical Reagent Corporation, China) were used for sample synthesis. That is, 24.0 mmol of A-site cation nitrate and 19.6 mmol of $SnCl_4\cdot5H_2O$ were added to 50 mL of deionized water. After stirring the mixed solution at room temperature for 1 h, 8 mol/L KOH was added to regulate the pH to 14. The resulting solution was stirred for 30 min, after which it was

transferred to a 100 mL Teflon-lined stainless-steel autoclave and subjected to a hydrothermal reaction at 200 °C for 24 h. The resultant precipitate was washed with deionized water until the concentration of total dissolved solids (TDS) in the filtrate remained below 10 ppm. Subsequently, the precipitate was dried at 120 °C for 12 h and then calcined at 800 °C for 4 h in air to obtain the target samples. The synthesis methods of other catalysts are the same as those of these two representative catalysts.

Catalyst characterization and reaction performance evaluation
The characterization and reaction performance testing conditions of the catalysts can be found in the Supplementary Materials.

RESULTS AND DISCUSSION
Catalytic performance
The catalytic performance of the $ASnO_3$ (A = Ca, Sr, Ba) perovskite catalysts for OCM is shown in Supplementary Figure 1, demonstrating the following order based on CH_4 conversion, C_2 selectivity, and C_2 yield at 600-650 °C: $BaSnO_3$ >$CaSnO_3$ > $SrSnO_3$. However, after $BaSnO_3$ achieves its maximum C_2 yield at 700 °C, the catalytic performance shows the following order: $SrSnO_3$ >$CaSnO_3$ >$BaSnO_3$. The O_2 conversion is ~95% using $BaSnO_3$ at 600 °C, whereas 100% O_2 conversion is achieved using $CaSnO_3$ or $SrSnO_3$ at 800 °C. Below 800 °C, O_2 conversion always obeys the following order: $CaSnO_3$ > $SrSnO_3$.

The catalytic performance of the $Ln_2Sn_2O_7$ (Ln = La, Pr, Nd) catalysts for OCM is shown in Supplementary Figure 2. Supplementary Figure 2A shows that the CH_4 conversion only changes slightly with increasing temperature, exhibiting the following order: $Nd_2Sn_2O_7$ > $Pr_2Sn_2O_7$ > $La_2Sn_2O_7$. Supplementary Figure 2B shows that the O_2 conversion is ~100% at 600 °C. With a rise in reaction temperature, oxygen is consumed completely; thus, the CH_4 conversion changes slightly with an increase in temperature. As pyrochlores have an intrinsic oxygen vacancy[29,30], they achieve an oxygen conversion of ~100% at 600 °C. Supplementary Figure 2C shows that the CO_x selectivity of pyrochlores does not differ significantly with temperature changes. Based on their high reaction performance, we selected the $SrSnO_3$ perovskite and $Nd_2Sn_2O_7$ pyrochlore as the subjects for further study to determine their structure-reactivity relationships.

The results of $SrSnO_3$ perovskite and $Nd_2Sn_2O_7$ pyrochlore reaction performance with increasing temperature are shown in Figure 1A-D. With the rise in reaction temperature, the conversions of CH_4 and O_2, C_2 selectivity, and C_2 yield of $SrSnO_3$ also escalate, and C_2 hydrocarbon is the main product. $SrSnO_3$ shows the best catalytic performance, achieving a CH_4 conversion of 25.3%, O_2 conversion of 99.9%, C_2 selectivity of 55.7%, and C_2 yield of 14.1%. Although the conversions of CH_4 and O_2 and the CO_x selectivity are less affected by temperature and the main product is CO_x, the C_2 yield of the $Nd_2Sn_2O_7$ catalyst is lower than 1% at 800 °C. The $SrSnO_3$ perovskite with the best reaction performance underwent a long-term stability test at 800 °C for 100 h [Figure 1E]; the results showed that the reaction performance did not decrease.

Temperature-programmed surface reaction (TPSR)-mass spectrometry (MS) was used in combination with online gas chromatography to investigate the effect of temperature on the catalytic performance of the two types of composite oxides for OCM reaction. Figure 2A shows that the main products (C_2 hydrocarbons) are generated after OCM is performed using a $SrSnO_3$ catalyst. Figure 2B shows that the primary reaction products are CO_x for $Nd_2Sn_2O_7$ catalyst, and the amount of C_2 hydrocarbons is extremely low. Table 1 shows that the onset temperature associated with deep methane oxidation is lower than the temperature required for the formation of C_2 hydrocarbons, indicating that the two reactions may take place at different active sites.

Table 1. Onset temperature of major products generated using different catalysts

Samples	Onset temperature of major products (°C)			
	CO_2	CO	C_2H_4	C_2H_6
$SrSnO_3$	575	470	660	660
$Nd_2Sn_2O_7$	375	450	646	646
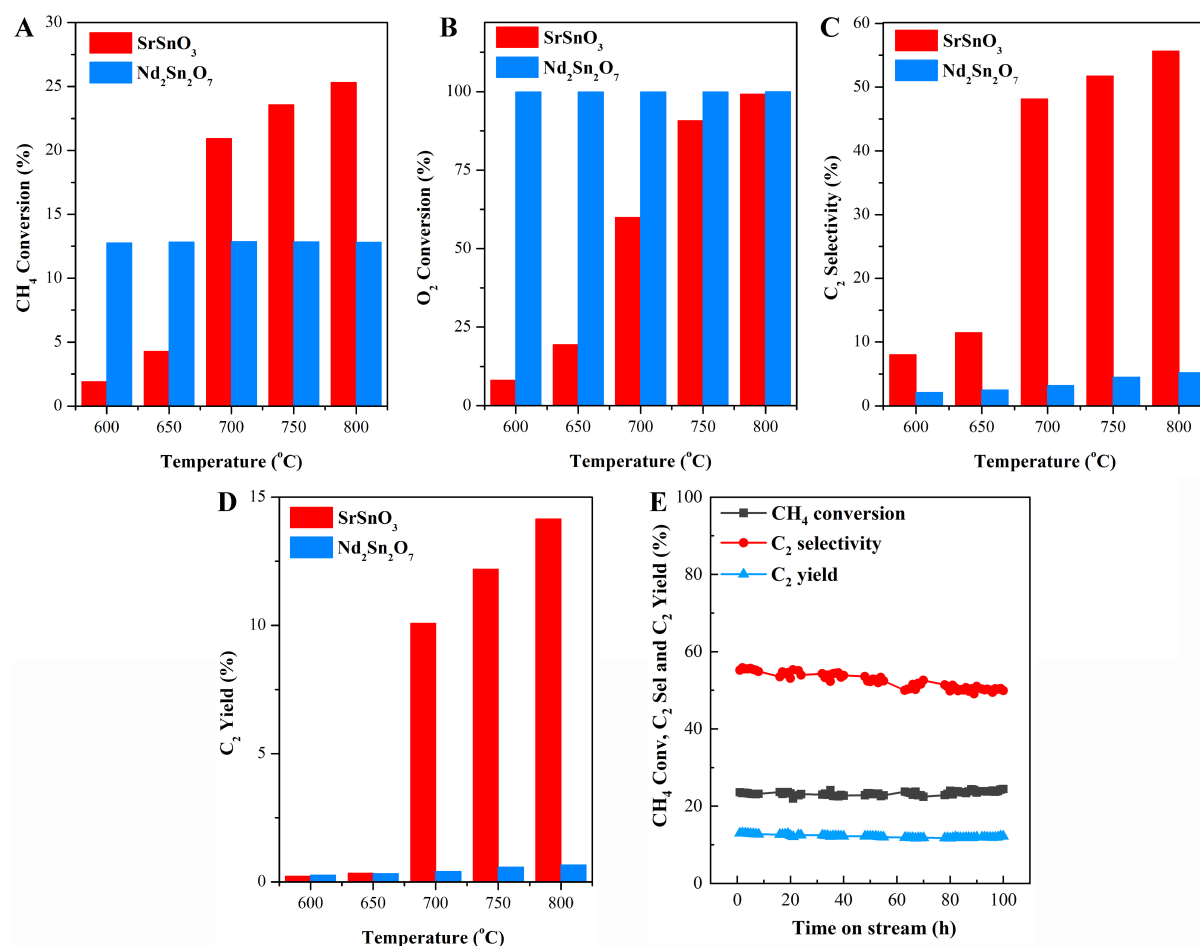
Figure 1. OCM reaction performance of the $SrSnO_3$ and $Nd_2Sn_2O_7$ catalysts. (A) CH_4 conversion; (B) O_2 conversion; (C) C_2 selectivity; and (D) C_2 yield. (E) Long-term stability test of $SrSnO_3$ catalyst at 800 °C for 100 h. Reaction conditions: $CH_4/O_2/Ar$ = 4/1/5, WHSV = 18,000 mL·h^{-1}·g^{-1}. OCM: Oxidative coupling of methane; WHSV: weight hourly space velocity.

Structural identification

The description of the X-ray diffraction (XRD) analysis can be found in the Supplementary Materials. Supplementary Figures 3-5 and Supplementary Table 1 reveal that two different types of pure-phase composite oxide catalysts were synthesized, and there was no phase change due to the OCM reaction. All $ASnO_3$ (A = Ca, Sr, Ba) and $Ln_2Sn_2O_7$ (Ln = La, Pr, Nd) catalysts had a specific surface area of 5-12 m^2/g, and there was no significant change after the reaction. The A/B atomic ratio was less than 1.00. The physicochemical properties of $SrSnO_3$ and $Nd_2Sn_2O_7$ composite oxide catalysts are shown in Table 2. $SrSnO_3$ exhibits an orthorhombic crystalline phase, and $Nd_2Sn_2O_7$ possesses a cubic crystalline phase.

Table 2. Physico-chemical properties of the composite oxide catalysts

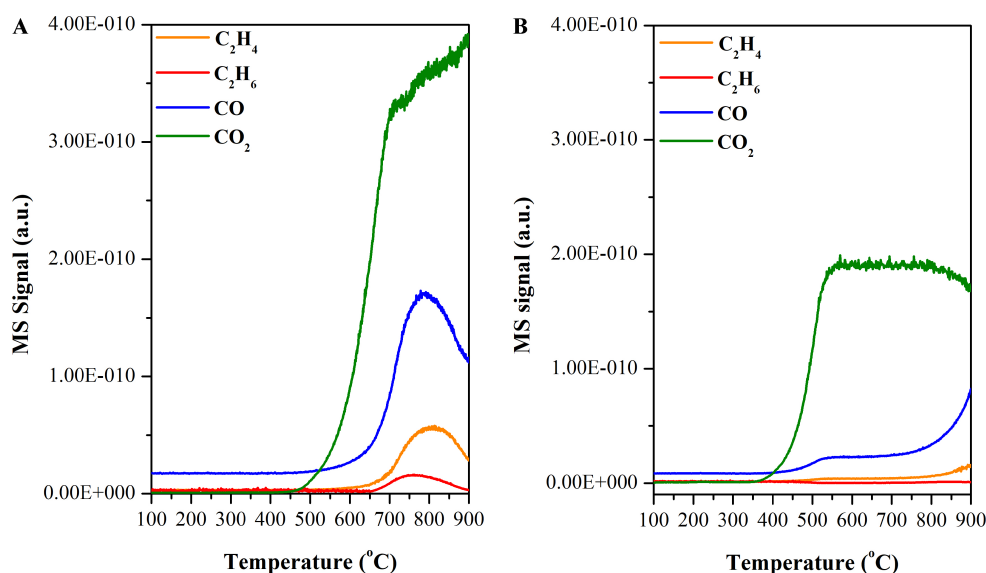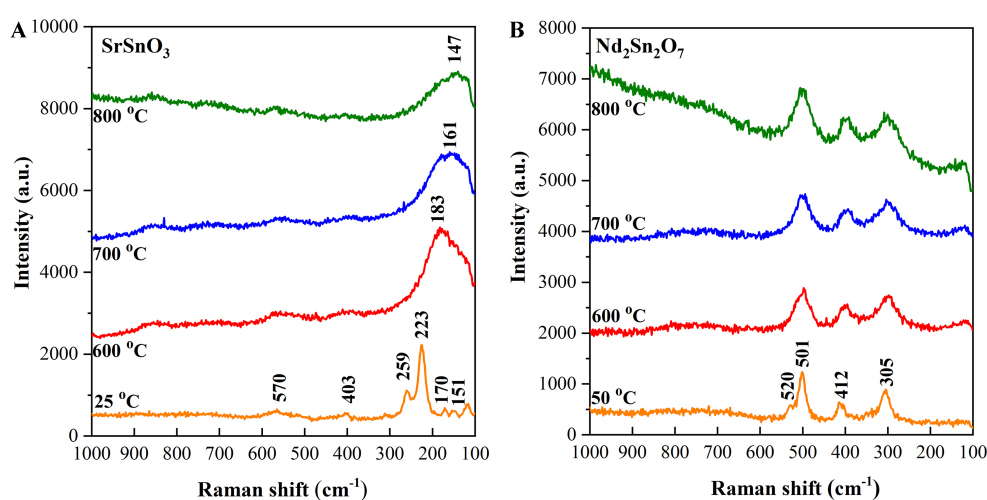| Samples	Crystalline phase	Lattice parameters				Specific surface areas (m²/g)		A/B atomic ratio
		a (Å)	b (Å)	c (Å)	α, β, γ (°)	Fresh	Spent	
$SrSnO_3$	Orthorhombic	5.710	5.723	8.067	90, 90, 90	6.4	5.9	0.94
$Nd_2Sn_2O_7$	Cubic	10.576	10.576	10.576	90, 90, 90	10.5	9.9	0.95

Figure 2. CH_4-TPSR-MS results in the presence of gaseous O_2 over the (A) $SrSnO_3$ and (B) $Nd_2Sn_2O_7$. Reaction conditions: $CH_4/O_2/He = 4/1/5$, (Ar as balance gas), WHSV = 18,000 mL·h⁻¹·g⁻¹. TPSR: Temperature-programmed surface reaction; MS: mass spectrometry; WHSV: weight hourly space velocity.

Compared with XRD, Raman spectroscopy is a more sensitive probe of structural distortions, short-range order, and symmetry in solids, providing structural information concerning the long-range order of metal oxides[31]. Raman spectra of the fresh catalysts displayed in Supplementary Figure 6 and the attribution of their Raman modes shown in Supplementary Tables 2 and 3 further testify that these two series of pure phase composite oxides have been successfully synthesized. To investigate the crystalline phase transition of these catalysts under OCM reaction conditions, *in situ* Raman spectra have been obtained, and the results are displayed in Supplementary Figures 7 and 8, and Figure 3. The catalyst was pretreated at 800 °C under a pure He atmosphere for 30 min, which was then cooled to room temperature. Next, the $CH_4/O_2/Ar = 4/1/5$ gas was introduced, and Raman spectra of the catalysts were recorded at 25, 600, 700, and 800 °C, respectively.

The frequencies of Raman signals corresponding to $SrSnO_3$ and $Nd_2Sn_2O_7$ at room temperature are shown in Table 3[32,33]. Figure 3A shows that as the temperature increases, the Raman bands of $SrSnO_3$ from 100 to 300 cm⁻¹ gradually widen and disappear. Meanwhile, only one broadband is observed when the temperature exceeds 600 °C. Considering that the crystalline phase of $SrSnO_3$ undergoes a transition from the *Pnma* orthorhombic phase to the *Imma* orthorhombic phase within this temperature range, the wide peak at 700-800 °C represents the Raman band of the *Imma* orthorhombic phase[34]. The change in symmetry of perovskite crystals may lead to lattice distortion, resulting in the generation of oxygen vacancies. Figure 3B shows that the Raman peaks of $Nd_2Sn_2O_7$ pyrochlore mostly remain unchanged, except for the peak broadening caused by thermal lattice expansion at high temperatures. This indicates that the $Nd_2Sn_2O_7$

Table 3. Raman shifts (cm^{-1}) of the active modes for SrSnO$_3$ and Nd$_2$Sn$_2$O$_7$ at room temperature

	Raman shifts (cm^{-1})	Assigned mode
SrSnO$_3$[32]	151	B$_{2g}$
	170	A$_g$
	223	A$_g$ Mode of the Sn-O-Sn groups along the c axis
	259	A$_g$ O-Sn-O bending in the ab plane and Sn-O-Sn scissoring perpendicular to the c axis
	403	-
	575	Sn-O$_3$ vibration band
Nd$_2$Sn$_2$O$_7$[33]	305	E$_g$
	412	F$_{2g}$
	501	A$_g$

Figure 3. *In situ* Raman spectra of (A) SrSnO$_3$ and (B) Nd$_2$Sn$_2$O$_7$ samples.

pyrochlore does not undergo a phase transition or lattice distortion at temperatures required for OCM. Supplementary Figure 7 demonstrates that CaSnO$_3$ did not undergo any crystal phase transition in the OCM reaction temperature range, while BaSnO$_3$ underwent a crystal phase transition from defective BaSnO$_3$ to regular cubic BaSnO$_3$ accompanied by the disappearance of oxygen vacancies at temperatures above 700 °C. This well explains the decrease in reaction performance of BaSnO$_3$ at temperatures above 700 °C. Supplementary Figure 8 confirms that La$_2$Sn$_2$O$_7$ and Pr$_2$Sn$_2$O$_7$ do not undergo crystal phase changes during the OCM reaction. As shown in Supplementary Figure 9, the Raman modes of the two series of composite oxides before and after the reaction did not change, which agrees well with the XRD results, further indicating that these two series of composite oxides are chemically stable.

We have also provided the XRD pattern of SrSnO$_3$ after stability testing in Supplementary Figure 10. The XRD pattern did not observe any diffraction peaks of other impurity peaks, indicating that the bulk structure of the perovskite is stable during stability testing.

Temperature-programmed desorption studies
As previously reported, the acid-base and oxygen properties on a catalyst surface are closely related to its catalytic performance for OCM[35-38]. Generally, moderate and strong acidic sites promote deep hydrocarbon

oxidation, whereas moderate and strong basic sites favor C_2 selectivity[39-41]. For different types of metal oxides, chemisorbed oxygen, such as O_2^-, O_2^{2-}, O^- and surface lattice O^{2-}, may be considered the OCM-selective oxygen species[42-46]. To investigate the effect of these active sites on the catalytic performance for OCM, $ASnO_3$ and $Ln_2Sn_2O_7$ catalysts have been characterized using carbon dioxide temperature-programmed desorption (CO_2-TPD), ammonia temperature-programmed desorption-mass spectrometry (NH_3-TPD-MS), and oxygen temperature-programmed desorption-mass spectrometry (O_2-TPD-MS). As shown in Supplementary Figures 11 and 12, and Supplementary Tables 4-6, as well as the discussion of the acid-base sites and reactive oxygen species of $ASnO_3$ and $Ln_2Sn_2O_7$ series in the supplementary materials, it can be concluded that it is reasonable to select $SrSnO_3$ and $Nd_2Sn_2O_7$ as typical examples of two composite oxides to explore surface reactive sites.

CO_2-TPD profiles of $SrSnO_3$ and $Nd_2Sn_2O_7$ catalysts are shown in Figure 4A, and the quantitative results are listed in Supplementary Table 4. According to the number of moderate and strong basic sites (the CO_2 desorption peak at 300-600 °C), $SrSnO_3$ (0.10 μmol/m²) > $Nd_2Sn_2O_7$ (0.01 μmol/m²), demonstrating that the number of basic sites favorable for the formation of C_2 hydrocarbons is higher in perovskites than that in pyrochlores.

NH_3-TPD-MS profiles of $SrSnO_3$ and $Nd_2Sn_2O_7$ are shown in Figure 4B, and the quantitative results are listed in Supplementary Table 5. $Nd_2Sn_2O_7$ exhibits a higher number of moderate acidic sites (the NH_3 desorption peak at 200-500 °C, 0.04 mmol/m²) than $SrSnO_3$ (0.01 mmol/m²). Table 2 shows that the A/B atomic ratios of $SrSnO_3$ and $Nd_2Sn_2O_7$ are similar, indicating that the factors affecting their acidic and basic sites are unrelated to the enrichment of surface Sn elements.

O_2-TPD-MS profiles of $SrSnO_3$ and $Nd_2Sn_2O_7$ are shown in Figure 4C, and the quantitative results are listed in Supplementary Table 6. Notably, $SrSnO_3$ perovskite exhibits a higher desorption temperature and chemisorbs more oxygen species than $Nd_2Sn_2O_7$ pyrochlores, indicating that both $SrSnO_3$ and $Nd_2Sn_2O_7$ have different mechanisms for activating gas-phase oxygen.

The results indicate that $SrSnO_3$ with the perovskite phase has more abundant moderate and strong basic sites, chemisorbed oxygen species, and fewer moderate acidic sites than $Nd_2Sn_2O_7$ with the pyrochlore phase.

Reactive oxygen species identification
To clarify the role of chemisorbed oxygen species in the OCM reaction, CH_4-TPSR in the absence of O_2 and continuous CH_4-pulse tests have been conducted for $SrSnO_3$ and $Nd_2Sn_2O_7$ after the saturation of oxygen adsorption. In the TPSR tests, the two catalysts are treated with high-purity He to remove the impurities adsorbed on the catalyst surface, after which they are exposed to a 40% CH_4/He mixture to perform a temperature-programmed reaction. Figure 5A and B shows that in the absence of gaseous O_2, the main reaction product of $SrSnO_3$ and $Nd_2Sn_2O_7$ catalysts is CO_2, indicating that the surface lattice oxygen species lead to deep methane oxidation. The amount of CO_2 generated using $SrSnO_3$ is significantly less than that produced using $Nd_2Sn_2O_7$, indicating that the latter has a higher lattice oxygen content for deep methane oxidation than the former.

In the continuous CH_4-pulse tests, the two catalysts are pretreated using the same method. After adsorption saturation at 750 °C in a 10% O_2/Ar gas flow (30 mL/min), 10% CH_4-Ar is pulsed every 3 min through a 1 mL loop; the results are shown in Figure 5C and D. $SrSnO_3$ produces a considerable amount of C_2 after OCM, whereas $Nd_2Sn_2O_7$ generates a large amount of CO_2 and a negligible amount of C_2, suggesting that the
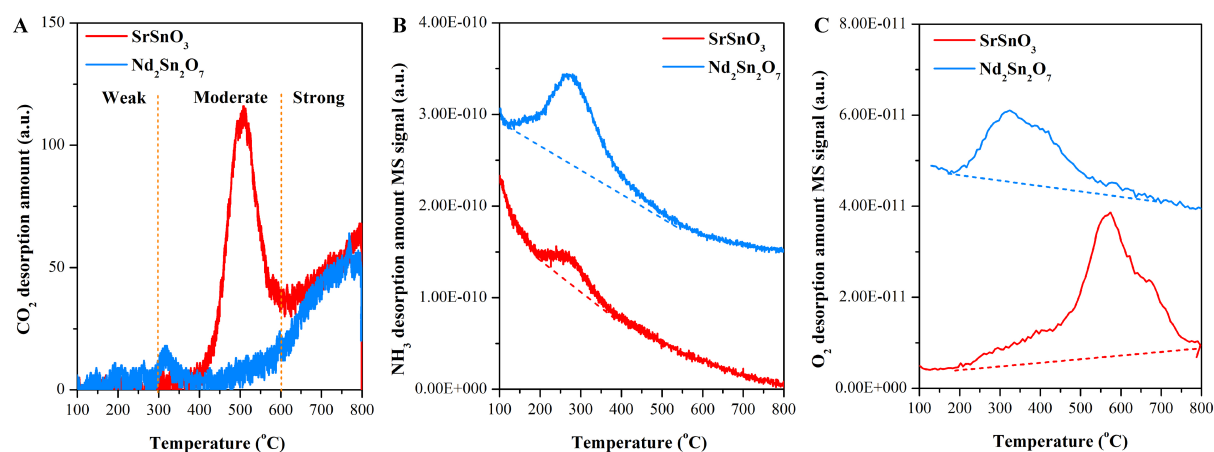
Figure 4. (A) CO_2-TPD profiles; (B) NH_3-TPD-MS profiles; and (C) O_2-TPD-MS profiles. TPD: Temperature-programmed desorption; MS: mass spectrometry.
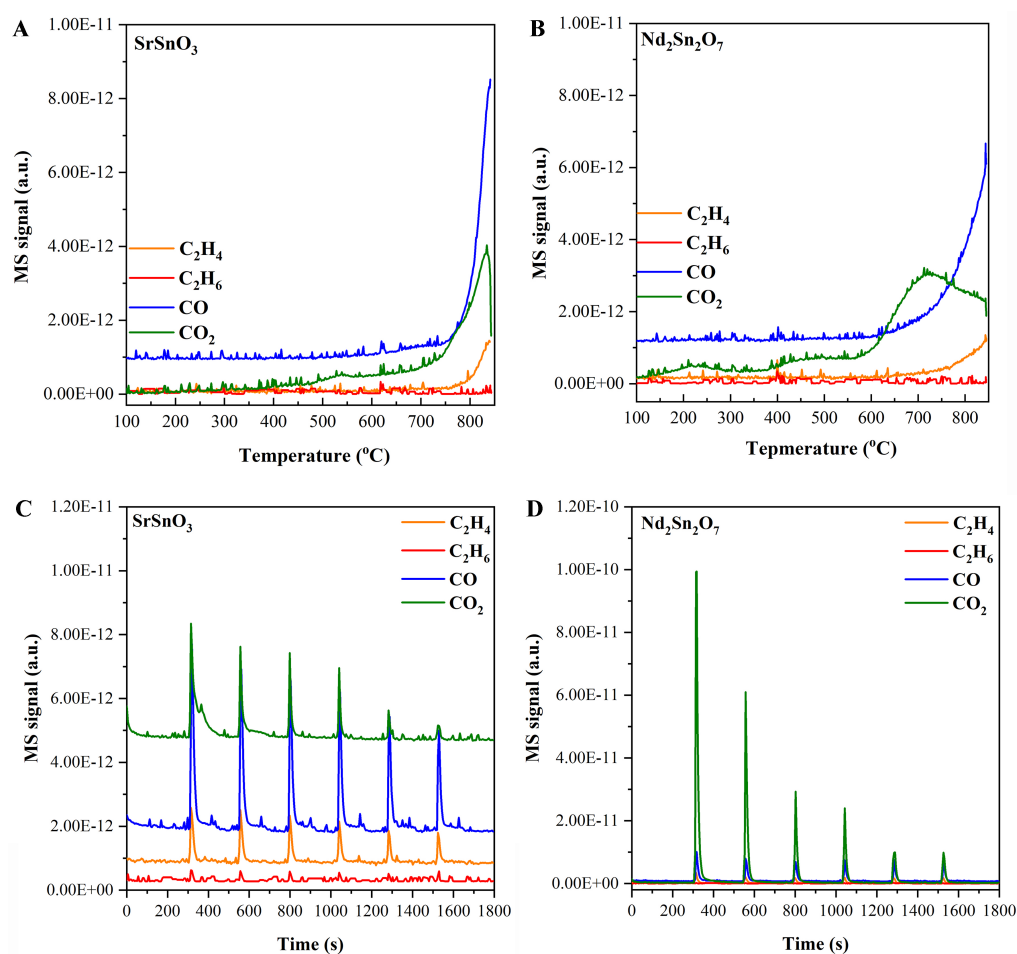
Figure 5. CH_4-TPSR-MS results in the absence of gaseous O_2 over (A) $SrSnO_3$ and (B) $Nd_2Sn_2O_7$. Reaction conditions: CH_4/He = 4/6, WHSV = 18,000 $mL \cdot h^{-1} \cdot g^{-1}$. CH_4-pulse tests performed over (C) $SrSnO_3$ and (D) $Nd_2Sn_2O_7$ after the saturation of oxygen adsorption. TPSR: Temperature-programmed surface reaction; MS: mass spectrometry; WHSV: .

oxygen species chemisorbed on the perovskite surface are the OCM-selective oxygen species. With an

increase in reaction time, the peak areas of all products gradually decrease.

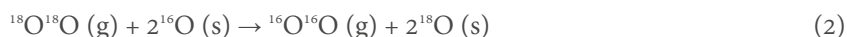Furthermore, the types of reactive oxygen species related to $SrSnO_3$ and $Nd_2Sn_2O_7$ have been examined by *in situ* X-ray photoelectron spectroscopy (XPS). The XPS O1s spectra of the two composite oxides are measured at room temperature, and then the samples are exposed to a 10% O_2-He gas mixture at 800 °C for 30 min. After being purged with high-purity He, the samples are allowed to cool to room temperature, and the spectra are collected again. As shown in Figure 6A and B, compared with the XPS O1s spectra obtained at room temperature, the peaks located at ~531 eV for both composite oxides decrease after the treatment with 10% O_2-He at 800 °C, which can be attributed to the decomposition of carbonate or dehydration hydroxyl groups on the catalyst surface. The remaining peak located at ~531 eV can be ascribed to the O_2^{2-} species[47]. In addition, the chemisorbed oxygen species on the surface of $SrSnO_3$ are more abundant than those on $Nd_2Sn_2O_7$.

To investigate the reactive oxygen exchange mechanisms of the two catalysts, isotope $^{18}O_2$ exchange experiments have been performed. As shown in Figure 7A and B, the products of both composite oxide catalysts are similar, indicating that the oxygen activation mechanisms of the two composite oxide catalysts are similar. Research has shown that the isotopic $^{18}O_2$ exchange mechanism of metal oxides involves the following two pathways[48,49]:

Simple hetero-exchange mechanism:

$$^{18}O^{18}O \text{ (g)} + {}^{16}O \text{ (s)} \rightarrow {}^{16}O^{18}O \text{ (g)} + {}^{18}O \text{ (s)} \tag{1}$$

Multiple hetero-exchange mechanism:

$$^{18}O^{18}O \text{ (g)} + 2{}^{16}O \text{ (s)} \rightarrow {}^{16}O^{16}O \text{ (g)} + 2{}^{18}O \text{ (s)} \tag{2}$$

In the present study, the main products of both composite oxides are $^{16}O^{16}O$, demonstrating that the activation of gas-phase oxygen in both composite oxides occurs via a multiple hetero-exchange mechanism. In addition, the generation of gas-phase oxygen $^{16}O^{16}O$ suggests the presence of binuclear oxygen species, such as O_2^- and O_2^{2-}[49], on the catalyst surface, which is consistent with the *in situ* XPS results, confirming that O_2^{2-} is the chemisorbed oxygen species of these two composite oxides.

Overall, the results reveal that the chemisorbed selective oxygen species produced most by the two composite oxides in the OCM reaction process is O_2^{2-}, which is activated through a multiple hetero-exchange mechanism.

Sn–O bond properties investigation

We use infrared (IR) spectra and XRD Rietveld refinement to investigate the Sn–O bond properties of both these composite oxides. In Figure 8A, the IR bands at 665 and 621 cm^{-1} are attributed to the stretching vibrations of the Sn–O bond for $SrSnO_3$ and $Nd_2Sn_2O_7$, respectively[33,50]. In addition, the IR peaks around 3,000 cm^{-1} are ascribed to surface hydroxyl groups[51], and the IR bands ranging from 1,000 to 1,500 cm^{-1} are related to surface carbonates[52,53]. Note that the IR peak intensity for the surface carbonate of $SrSnO_3$ is significantly stronger than that of $Nd_2Sn_2O_7$, which further suggests that the surface basic sites of $SrSnO_3$ are more abundant than those of $Nd_2Sn_2O_7$. Moreover, the B–O bond of $A_2B_2O_7$ and ABO_3 composite oxides have covalent bonding properties, making the B–O bond more prone to fracture than the A–O bond with ionic bonding properties[54,55]. From our calculations, the Sn–O bond force constant of $Nd_2Sn_2O_7$ pyrochlore

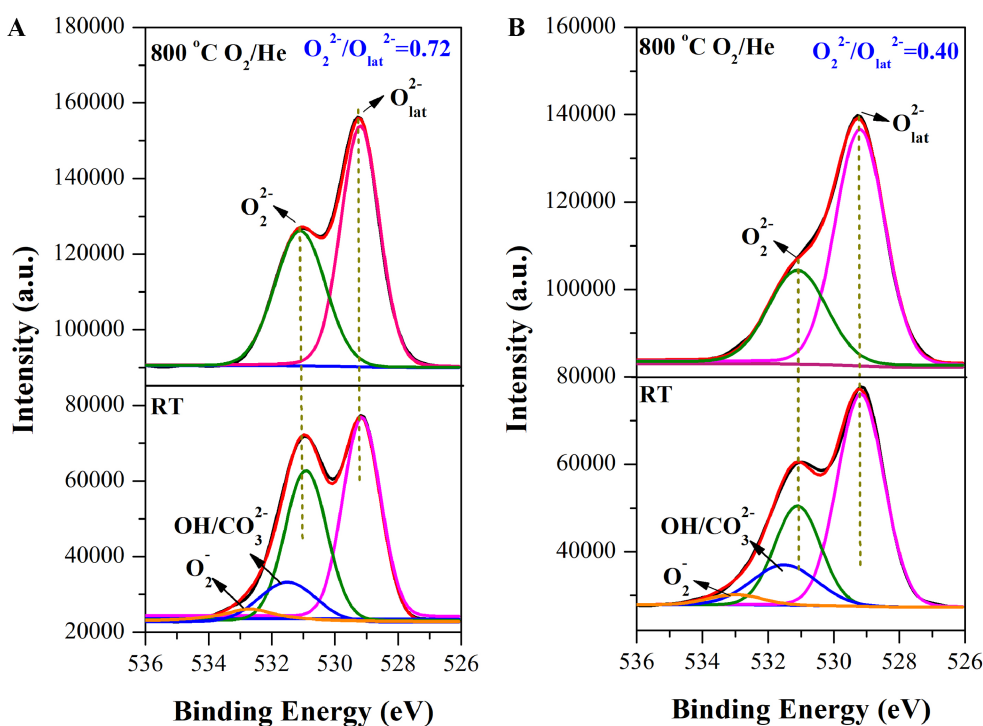**Figure 6.** *In situ* XPS O 1s spectra of the (A) $SrSnO_3$ and (B) $Nd_2Sn_2O_7$. XPS: X-ray photoelectron spectroscopy.
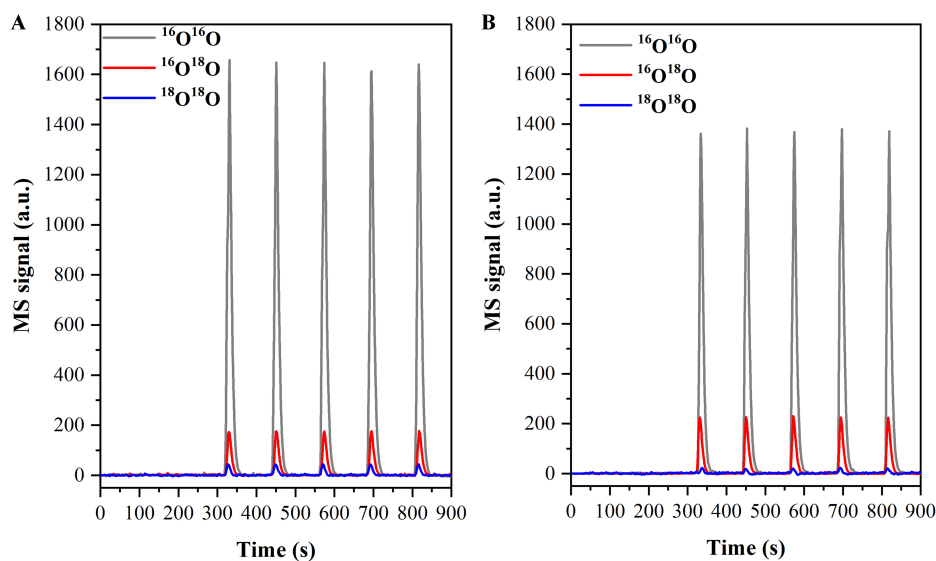
Figure 7. $^{18}O_2$ pulse reaction over the (A) $SrSnO_3$ and (B) $Nd_2Sn_2O_7$ catalysts at 800 °C.

(3.162 N/cm) is lower than that of $SrSnO_3$ perovskite (3.628 N/cm); the calculation method can be found in Supplementary Materials.

As shown in Supplementary Table 7, $SrSnO_3$ has three different Sn–O bond lengths, which is due to their orthorhombic crystal phases and inclination, twisting, or distortion of BO_6 octahedra, deviating from the cubic structure[56]. Conversely, the cubic $Nd_2Sn_2O_7$ pyrochlore has one Sn–O bond length longer than that of

Figure 8. (A) FT-IR spectra; (B) H_2-TPR profiles; and (C) EPR spectra of the catalysts. FT-IR: Fourier-transform infrared spectroscopy; TPR: ; EPR: electron paramagnetic resonance.

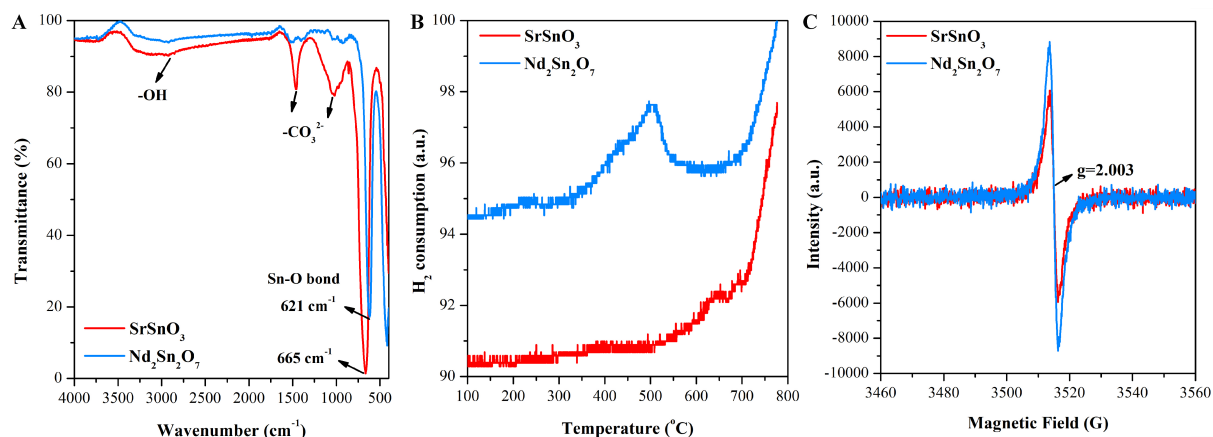perovskite, which is consistent with the fact that the Sn–O bond force constant of pyrochlore is smaller than that of perovskite. This conclusion can be further supported by the H_2-temperature-programmed reduction (TPR) results. As shown in Figure 8B, no reduction peaks are observed for $SrSnO_3$, but a peak attributed to the Sn–O bond reduction is observed around 500 °C for $Nd_2Sn_2O_7$[57,58]. Supplementary Figure 13A confirms that after the H_2-TPR reaction, the XRD diffraction peaks of $SrSnO_3$ did not change, while the XRD pattern of $Nd_2Sn_2O_7$ can be observed to belong to the diffraction peak of Nd_2O_3, indicating that the phase structure of $SrSnO_3$ under a strong reducing atmosphere of H_2 at high-temperature is stable, while $Nd_2Sn_2O_7$ can be partially reduced. The XRD, Raman spectroscopy, and XPS results of the fresh catalysts indicate that no residual SnO_2 content exists, and the H_2-TPR results testify that the Sn–O lattice oxygen structure of $Nd_2Sn_2O_7$ is looser than that of $SrSnO_3$.

Previous studies have found that weaker B–O bonds in $A_2B_2O_7$ composite oxides are easier to break, resulting in abundant oxygen vacancies[59]. Thus, $Nd_2Sn_2O_7$ is expected to have more abundant oxygen vacancies than $SrSnO_3$. In Figure 8C, the g value of 2.003 is attributed to the characteristic signal of oxygen vacancies[60,61], and the electron paramagnetic resonance (EPR) signal of $Nd_2Sn_2O_7$ is stronger than that of $SrSnO_3$, further demonstrating that $Nd_2Sn_2O_7$ has more abundant oxygen vacancies than $SrSnO_3$. EPR spectra of the spent catalysts displayed in Supplementary Figure 13B demonstrated that after OCM reaction, the oxygen vacancies of $Nd_2Sn_2O_7$ are still more abundant than those in $SrSnO_3$. Although $Nd_2Sn_2O_7$ has more oxygen vacancies than $SrSnO_3$, the previous results show that the amount of chemisorbed oxygen species in $SrSnO_3$ is higher than that in $Nd_2Sn_2O_7$. This indicates that the abundance of oxygen vacancies is not directly related to the amount of adsorbed oxygen species on the catalyst surface and may be influenced by other factors.

A brief discussion

During the OCM reaction, the $SrSnO_3$ sample mainly contains C_2 products, whereas the $Nd_2Sn_2O_7$ sample primarily contains CO_x products. The analysis of acid-base properties reveals that the number of moderate and strong basic sites is greater in $SrSnO_3$ than in $Nd_2Sn_2O_7$. Meanwhile, the number of acidic sites is inversely proportional to that of basic sites. The O_2-TPD-MS and *in situ* XPS O1s results indicate that their chemisorbed oxygen species (O_2^{2-}) are OCM-selective oxygen species and the amount of chemisorbed oxygen and O_2^{2-}/O^{2-} ratios are greater for $SrSnO_3$ than for $Nd_2Sn_2O_7$, but the desorption temperature of $SrSnO_3$ is higher than that of $Nd_2Sn_2O_7$. In addition, the Sn–O bond strength of $Nd_2Sn_2O_7$ is weaker than that of $SrSnO_3$, resulting in more abundant oxygen vacancies in $Nd_2Sn_2O_7$ than in $SrSnO_3$, which contradicts

the fact that the chemisorbed oxygen species on the surface of $SrSnO_3$ are more abundant than $Nd_2Sn_2O_7$.

Coordination unsaturated metal cations (acidic sites) are known to chemically adsorb the methyl radicals, ethyl radicals, and ethylene formed during OCM[62]. Consequently, a series of reactive oxygen species is generated via the activation of gas-phase oxygen, after which CO_x products are formed[62]. Therefore, the synergistic effect of acidic sites and reactive oxygen species (chemisorbed oxygen species or weakly bonded lattice oxygen) on the catalyst surface can lead to the generation of deep oxidation products. In addition, the weaker Sn–O bond in $Nd_2Sn_2O_7$ is easier to break during the OCM reaction, resulting in the generation of more acidic sites. Basic sites are generally composed of hydroxyl groups and coordination unsaturated basic lattice oxygen species[53]. These electron-rich/basic sites can provide electrons to stabilize electron-deficient oxygen species such as O_2^-, O_2^{2-}, and O^-.

As illustrated in Supplementary Table 8, the electronegativity of Sr and Nd elements is lower than that of Sn element; compared with Sr–O, Nd–O, and Sn–O bonds, the tendency of electrons from Sr and Nd elements to transfer to O element is greater than that of Sn element. Therefore, Sr–O and Nd–O bonds exhibit ionic bond properties, while Sn–O bonds exhibit covalent bond properties. The electronegativity of Sr element is smaller than that of Nd and Sn elements; the electron transfer of Sr element in the Sr–O bond tends to be stronger than that of Nd element in the Nd–O and Sn element in the Sn–O bond towards O. Therefore, the lattice oxygen basicity of the Sr–O bond is stronger than that of the Nd–O and Sn–O bonds. In addition, the sum of the electronegativity of $SrSnO_3$ metal elements ($\chi_{Sr} + \chi_{Sn} = 2.91$) is smaller than that of $Nd_2Sn_2O_7$ ($\chi_{Sr} + \chi_{Sn} = 3.10$), the ability of $SrSnO_3$ metal element electrons to transfer to oxygen is stronger than that of $Nd_2Sn_2O_7$, which well explains that the basic sites on the surface of $SrSnO_3$ are more abundant than $Nd_2Sn_2O_7$. As can be seen from the above analysis, the lattice oxygen of Sr–O is more electron rich than that of Nd–O and Sn–O bonds, so the basic lattice oxygen of Sr–O and Nd–O bonds can not only activate gas-phase oxygen to generate chemisorbed oxygen, but also stabilize these electron-deficient oxygen species on the surface of the catalyst.

Even though the surfaces of metal oxides are abundant in oxygen vacancies, which can create many electrophilic oxygen species, it is difficult to stabilize them on the surface when there are fewer basic sites[62]. This explains why, despite $Nd_2Sn_2O_7$ having more oxygen vacancies than $SrSnO_3$, there are fewer surface selective oxygen species O_2^{2-} for $Nd_2Sn_2O_7$ than for $SrSnO_3$. Moreover, studies have shown that the temperature at which methane combustion occurs at acidic sites is lower than the OCM reaction at basic sites on metal oxide catalysts[41]. This explains why the onset temperature is lower for generating CO_x than for generating C_2 products.

Considering the crystalline phase structure and high-temperature crystalline phase transition of the two composite oxides, it is important to note that $Nd_2Sn_2O_7$ possesses intrinsic oxygen vacancies, and thus, the chemisorbed oxygen species are directly activated by oxygen vacancies, generating chemisorbed oxygen species at low temperatures. Therefore, the desorption temperature is lower for $Nd_2Sn_2O_7$. At high temperatures, $SrSnO_3$ undergoes lattice distortion[63], resulting in thermal defects such as oxygen vacancies. Hence, gas-phase oxygen is only activated to produce chemisorbed oxygen species at higher temperatures, resulting in a higher desorption temperature. The different desorption temperatures of chemisorbed oxygen species in the two composite oxides are attributed to their various gas-phase oxygen activation pathways.

The BO_6 octahedra of perovskite are connected through corner-sharing to form a three-dimensional network [Scheme 2A][12], and the octahedra are stacked closely. According to the Pauling coordination polyhedron connection rules, the close corner-sharing of the octahedra leads to the maximum distance

A

B

Perovskite   **Pyrochlore**
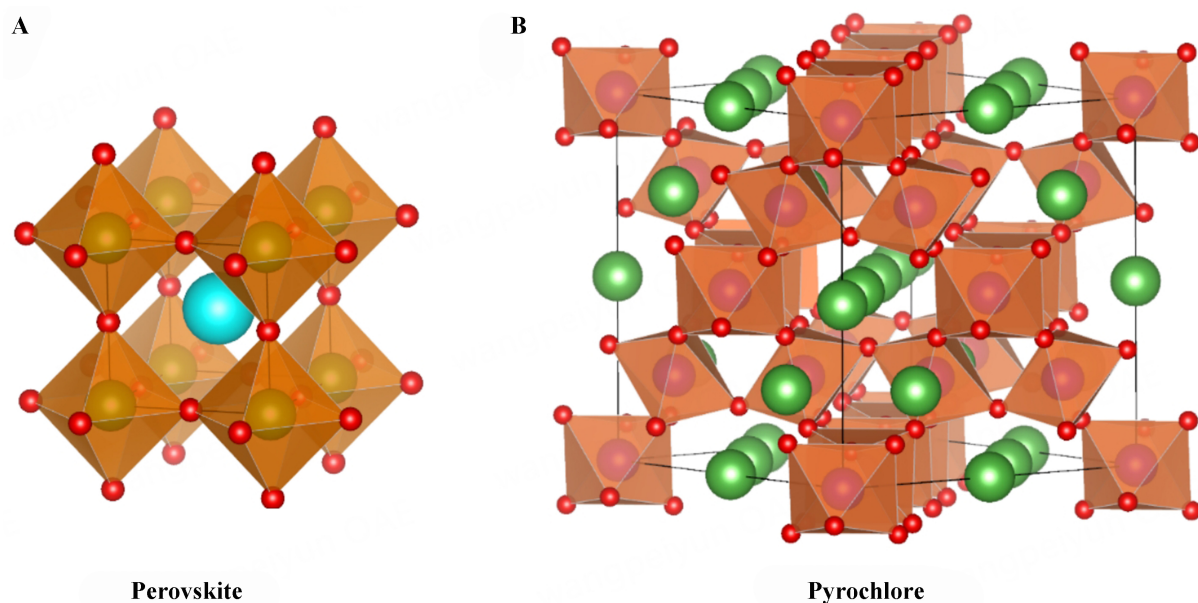
Scheme 2. The network of corner-sharing octahedra BO_6 formed in (A) perovskite and (B) pyrochlore structure.

between positive cations and smaller Coulomb repulsion. In addition, this compact and symmetrical stacking mode makes the cations at the B-site subject to the Coulomb interaction between electrons, the effect of the surrounding oxygen ionic crystal field, and the spin-spin interaction within the atom, which balance each other to reach the most stable state. Compared with the close octahedra stacking of perovskite, the BO_6 octahedra stacking of pyrochlore is looser and more disordered [Scheme 2B]. This disorderly and loose stacking mode leads to different effects on some B-site cations, and they cannot balance each other. Therefore, the B–O bond of pyrochlore is weaker than that of perovskite, and it is easier to break.

From the results, the variations in the degrees of lattice oxygen relaxation and acidic sites between perovskite and pyrochlore may be caused by the different packing modes of BO_6 octahedra. BO_6 octahedra in perovskite are more tightly packed than those in pyrochlore. Therefore, the B–O bond in perovskite is less easily reduced and less easily broken to produce acidic sites than that in pyrochlore.

CONCLUSIONS

In summary, we synthesized two types of composite oxides ($SrSnO_3$ and $Nd_2Sn_2O_7$) with definite structures via a hydrothermal method for OCM catalysis. Furthermore, we compared and analyzed the differences in their active sites using various characterization methods. The $SrSnO_3$ perovskite catalyst mainly produces C_2 hydrocarbons during the OCM reaction, whereas the $Nd_2Sn_2O_7$ pyrochlore catalyst primarily generates CO_x products.

$SrSnO_3$ perovskite has abundant basic sites that produce a synergistic effect with chemisorbed oxygen species of O_2^{2-}, which, in turn, facilitates the formation of C_2 products. The thermal defects generated by the high-temperature lattice distortion of perovskites (such as oxygen vacancies that lead to the formation of chemisorbed oxygen species) play an important role in the generation of C_2 hydrocarbons. When an appropriate number of basic sites exist along with abundant chemisorbed oxygen species, perovskites exhibit a high selectivity and yield of C_2. For $Nd_2Sn_2O_7$ pyrochlore, the synergistic effect of the abundant acidic sites on their surfaces and the reactive oxygen species (chemisorbed oxygen species) generated by

intrinsic oxygen vacancies and weakly bonded lattice oxygen mainly results in the formation of CO_x products. The Sn–O bond strength of pyrochlore is the main factor affecting the formation of deep oxidation products (CO_x). The weaker the Sn–O bond, the higher the number of acid sites, and the higher the CO_x selectivity.

The oxygen vacancies of both composite oxides are related to the Sn–O bonds. The weaker the Sn–O bond of the composite oxides, the richer the oxygen vacancies. However, the amount of chemisorbed oxygen species is not only related to oxygen vacancies but also to basic sites. Composite oxides generally have abundant oxygen vacancies and fewer basic sites, resulting in a lower amount of electrophilic oxygen species stabilized on the catalyst surface. Basic sites have a stronger impact on the amount of chemisorbed oxygen species than oxygen vacancies.

The Sn–O bond strength and the compactness of the $[SnO_6]$ octahedron are responsible for the differences in the catalytic performance of $SrSnO_3$ and $Nd_2Sn_2O_7$ for OCM. Pyrochlores have a weak Sn–O bond strength, and their $[SnO_6]$ octahedra are loosely stacked. Thus, Sn–O bonds break easily and acidic sites are readily generated. Moreover, because lattice oxygen can be easily reduced and its mobility is high, CO_x products are primarily formed in pyrochlores; meanwhile, contrasting results are observed for perovskites.

DECLARATIONS

Authors' contributions
Data curation, investigation, software: Ouyang R, Zhong Xs, Gong Y, Liu Y
Project administration, supervision, software: Fang X, Shen J
Conceptualization, funding acquisition, investigation, methodology, project administration, resources, supervision, validation, writing - review and editing: Wang X, Xu J

Availability of data and materials
Detailed experimental procedures and related data were published as Supplementary Materials in the journal, and the data supporting the findings of this study are available within its Supplementary Materials.

Financial support and sponsorship

Conflicts of interest
All authors declared that there are no conflicts of interest.

Ethical approval and consent to participate
Not applicable.

Consent for publication
Not applicable.

Copyright

REFERENCES
1. Doherty CJ, Kay SA. Circadian surprise - it's not all about transcription. *Science* 2012;338:338-40. DOI PubMed
2. Hammond C, Conrad S, Hermans I. Oxidative methane upgrading. *ChemSusChem* 2012;5:1668-86. DOI PubMed

3.   Qiu X, Wong N, Tin K, Zhu Q. Review low temperature catalysts for oxidative coupling of methane. *J Chem Technol Biotechnol* 1996;65:303-8. DOI

4.   Thybaut J, Marin G, Mirodatos C, et al. A novel technology for natural gas conversion by means of integrated oxidative coupling and dry reforming of methane. *Chem Ing Tech* 2014;86:1855-70. DOI

5.   Aljama H, Nørskov JK, Abild-pedersen F. Tuning methane activation chemistry on alkaline earth metal oxides by doping. *J Phys Chem C* 2018;122:22544-8. DOI

6.   Zhou X, Pang Y, Liu Z, et al. Active oxygen center in oxidative coupling of methane on La_2O_3 catalyst. *J Energy Chem* 2021;60:649-59. DOI

7.   Si J, Sun W, Zhao G, Lu Y. Support oxide tuning of MnO_x-Na_2WO_4 catalysts enables low-temperature light-off of OCM. *Fuel* 2022;311:122539. DOI

8.   Hiyoshi N, Ikeda T. Oxidative coupling of methane over alkali chloride–Mn–Na_2WO_4/SiO_2 catalysts: promoting effect of molten alkali chloride. *Fuel Process Technol* 2015;133:29-34. DOI

9.   Lim S, Choi J, Jin Suh D, Lee U, Song KH, Ha J. Low-temperature oxidative coupling of methane using alkaline earth metal oxide-supported perovskites. *Catal Today* 2020;352:127-33. DOI

10.   Roger A, Petit C, Kiennemann A. Effect of metallo-organic precursors on the synthesis of Sm–Sn pyrochlore catalysts: application to the oxidative coupling of methane. *J Catal* 1997;167:447-59. DOI

11.   Murthy PR, Liu Y, Wu G, Diao Y, Shi C. Oxidative coupling of methane: perspective for high-value C_2 chemicals. *Crystals* 2021;11:1011. DOI

12.   Mi J, Chen J, Chen X, Liu X, Li J. Recent status and developments of vacancies modulation in the ABO_3 perovskites for catalytic applications. *Chemistry* 2023;29:e202202713. DOI PubMed

13.   Deng J, Chen P, Xia S, et al. Advances in oxidative coupling of methane. *Atmosphere* 2023;14:1538. DOI

14.   Fisher JG, Rout D, Moon K, Kang SL. High-temperature X-ray diffraction and Raman spectroscopy study of $(K_{0.5}Na_{0.5})NbO_3$ ceramics sintered in oxidizing and reducing atmospheres. *Mater Chem Phys* 2010;120:263-71. DOI

15.   Kapusta B, Guillopé M. Molecular dynamics study of the perovskite $MgSiO_3$ at high temperature: structural, elastic and thermodynamical properties. *Phys Earth Planet In* 1993;75:205-24. DOI

16.   Gao L, Liang K, Liu Z, Chen H, Zhang J. Structure dependence of dielectric properties in Ca-doped bismuth magnesium niobate pyrochlores. *J Alloys Compd* 2022;922:165859. DOI

17.   Muñoz HJ, Korili SA, Gil A. Progress and recent strategies in the synthesis and catalytic applications of perovskites based on lanthanum and aluminum. *Materials* 2022;15:3288. DOI PubMed PMC

18.   Renju UA, Prabhakar Rao P, Vaisakhan Thampi DS. Influence of phase transition from order to disorder and Philip's ionicity on the thermal expansion coefficient of pyrochlore type compositions with a multivalent environment. *New J Chem* 2017;41:245-55. DOI

19.   Behara S, Poonawala T, Thomas T. Crystal structure classification in ABO_3 perovskites via machine learning. *Comput Mater Sci* 2021;188:110191. DOI

20.   Liu H, Cheng J, Dong H, et al. Screening stable and metastable ABO_3 perovskites using machine learning and the materials project. *Comput Mater Sci* 2020;177:109614. DOI

21.   Jerez A, López ML, García-Martín S, Veiga ML, Pico C. Defect pyrochlore structure $A_2B_2X_6$: a general approach to the coordination polyhedra around the metal ions. *J Mater Sci* 1991;26:5163-6. DOI

22.   Jerpoth SS, Iannello J, Aboagye EA, Yenkie KM. Computer-aided synthesis of cost-effective perovskite crystals: an emerging alternative to silicon solar cells. *Clean Technol Envir* 2020;22:1187-98. DOI

23.   Subramanian M, Aravamudan G, Subba Rao G. Oxide pyrochlores - A review. *Prog Solid State Ch* 1983;15:55-143. DOI

24.   Shamblin J, Tracy CL, Ewing RC, et al. Structural response of titanate pyrochlores to swift heavy ion irradiation. *Acta Mater* 2016;117:207-15. DOI

25.   Petit C, Teymouri M, Roger A, Rehspringer J, Hilaire L, Kiennemann A. Preparation and characterization of $ASnO_3$ (A=Ca, Sr or Ba) tin compounds for methane oxidative coupling. *Stud Surf Sci Catal* 1995;91:607-16. DOI

26.   Park S, Hwang HJ, Moon J. Catalytic combustion of methane over rare earth stannate pyrochlore. *Catal Lett* 2003;87:219-23. DOI

27.   Yang W, Yan Q, Fu X. Oxidative coupling of methane over Sr−Ti, Sr−Sn perovskites and corresponding layered perovskites. *React Kinet Catal Lett* 1995;54:21-7. DOI

28.   Cheng J, Wang H, Hao Z, Wang S. Catalytic combustion of methane over cobalt doped lanthanum stannate pyrochlore oxide. *Catal Commun* 2008;9:690-5. DOI

29.   Lumpkin GR, Aughterson RD. Perspectives on pyrochlores, defect fluorites, and related compounds: building blocks for chemical diversity and functionality. *Front Chem* 2021;9:778140. DOI PubMed PMC

30.   Beyerlein R, Horowitz H, Longo J, Leonowicz M, Jorgensen J, Rotella F. Neutron diffraction investigation of ordered oxygen vacancies in the defect pyrochlores, $Pb_2Ru_2O_{6.5}$ and $PbT_1Nb_2O_{6.5}$. *J Solid State Chem* 1984;51:253-65. DOI

31.   Moncada J, Adams WR, Thakur R, Julin M, Carrero CA. Developing a Raman spectrokinetic approach to gain insights into the structure–reactivity relationship of supported metal oxide catalysts. *ACS Catal* 2018;8:8976-86. DOI

32.   Alammar T, Hamm I, Grasmik V, Wark M, Mudring AV. Microwave-assisted synthesis of perovskite $SrSnO_3$ nanocrystals in ionic liquids for photocatalytic applications. *Inorg Chem* 2017;56:6920-32. DOI PubMed

33.   Rajakumaran R, Balamurugan K, Chen SM, Sukanya R. Facile synthesis of neodymium stannate nanoparticles an effective electrocatalyst for the selective detection of dimetridazole in biological samples. *Anal Chim Acta* 2022;1190:339234. DOI PubMed

34. Cortés-adasme E, Castillo R, Conejeros S, Vega M, Llanos J. Behavior of Eu ions in $SrSnO_3$: optical properties, XPS experiments and DFT calculations. *J Alloys Compd* 2019;771:162-8. DOI

35. Wu T, Wei Y, Xiong J, et al. Atomically dispersed SrO_x species on exposed {2 2 2} facets of pyrochlore $La_2Zr_2O_7$ nanocrystals for boosting low-temperature oxidative coupling of methane. *Fuel* 2023;333:126479. DOI

36. Kim I, Lee G, Na HB, Ha J, Jung JC. Selective oxygen species for the oxidative coupling of methane. *Mol Catal* 2017;435:13-23. DOI

37. Thum L, Rudolph M, Schomäcker R, et al. Oxygen activation in oxidative coupling of methane on calcium oxide. *J Phys Chem C* 2019;123:8018-26. DOI

38. Jiang S, Ding W, Zhao K, et al. Enhanced chemical looping oxidative coupling of methane by Na-doped $LaMnO_3$ redox catalysts. *Fuel* 2021;299:120932. DOI

39. Yan L, Zhang J, Gao X, et al. Oxidative coupling of methane over Mo-Sn catalysts. *Chem Commun* 2021;57:13297-300. DOI PubMed

40. Zhao M, Ke S, Wu H, Xia W, Wan H. Flower-like $Sr-La_2O_3$ microspheres with hierarchically porous structures for oxidative coupling of methane. *Ind Eng Chem Res* 2019;58:22847-56. DOI

41. Papa F, Luminita P, Osiceanu P, Birjega R, Akane M, Balint I. Acid–base properties of the active sites responsible for C_2^+ and CO_2 formation over $MO–Sm_2O_3$ (M=Zn, Mg, Ca and Sr) mixed oxides in OCM reaction. *J Mol Catal A Chem* 2011;346:46-54. DOI

42. Gambo Y, Jalil A, Triwahyono S, Abdulrasheed A. Recent advances and future prospect in catalysts for oxidative coupling of methane to ethylene: a review. *J Ind Eng Chem* 2018;59:218-29. DOI

43. Gu S, Oh H, Choi J, et al. Effects of metal or metal oxide additives on oxidative coupling of methane using Na_2WO_4/SiO_2 catalysts: reducibility of metal additives to manipulate the catalytic activity. *Appl Catal A Gen* 2018;562:114-9. DOI

44. Yoon S, Lim S, Choi JW, Suh DJ, Song KH, Ha JM. Study on the unsteady state oxidative coupling of methane: effects of oxygen species from O_2, surface lattice oxygen, and CO_2 on the C_{2+} selectivity. *RSC Adv* 2020;10:35889-97. DOI PubMed PMC

45. Zanina A, Kondratenko VA, Lund H, et al. The role of adsorbed and lattice oxygen species in product formation in the oxidative coupling of methane over M_2WO_4/SiO_2 (M = Na, K, Rb, Cs). *ACS Catal* 2022;12:15361-72. DOI

46. Tang L, Yamaguchi D, Wong L, Burke N, Chiang K. The promoting effect of ceria on Li/MgO catalysts for the oxidative coupling of methane. *Catal Today* 2011;178:172-80. DOI

47. Pang Y, Zhou X, Vovk EI, et al. Understanding lanthanum oxide surface structure by DFT simulation of oxygen 1s calibrated binding energy in XPS after in situ treatment. *Appl Surf Sci* 2021;548:149214. DOI

48. Doornkamp C, Clement M, Ponec V. The isotopic exchange reaction of oxygen on metal oxides. *J Catal* 1999;182:390-9. DOI

49. Martin D, Duprez D. Mobility of surface species on oxides. 1. Isotopic exchange of $^{18}O_2$ with ^{16}O of SiO_2, Al_2O_3, ZrO_2, MgO, CeO_2, and $CeO_2-Al_2O_3$. Activation by noble metals. Correlation with oxide basicity. *J Phys Chem* 1996;100:9429-38. DOI

50. Chandra S, Ravichandran K, George G, Arun T, Rajkumar PV. Influence of Fe and Fe+F doping on the properties of sprayed SnO_2 thin films. *J Mater Sci Mater Electron* 2016;27:9558-64. DOI

51. Lopes LB, Vieira LH, Assaf JM, Assaf EM. Effect of Mg substitution on $LaTi_{1-x} Mg_xO_{3+\delta}$ catalysts for improving the C2 selectivity of the oxidative coupling of methane. *Catal Sci Technol* 2021;11:283-96. DOI

52. Gao W, Zhou T, Wang Q. Controlled synthesis of MgO with diverse basic sites and its CO_2 capture mechanism under different adsorption conditions. *Chem Eng J* 2018;336:710-20. DOI

53. Davydov A, Shepotko M, Budneva A. Basic sites on the oxide surfaces: their effect on the catalytic methane coupling. *Catal Today* 1995;24:225-30. DOI

54. Liu C, Li Y, Li Y, et al. First principle calculation of helium in $La_2Zr_2O_7$: effects on structural, electronic properties and radiation tolerance. *J Nucl Mater* 2018;500:72-80. DOI

55. Srivastava AM, Brik MG, Beers WW, Cohen WE. Luminescence of Mn^{4+} in the orthorhombic perovskites, $AZrO_3$ (A=Ca, Sr). *Opt Mater* 2021;114:110906. DOI

56. Antonio J, Muñoz H, Rosas-huerta J, et al. Effects of the phase transition on the structural, mechanical, electronic and vibrational properties of the $CaSnO_3$ perovskite: study under hydrostatic pressure. *J Phys Chem Solids* 2022;163:110594. DOI

57. Wang H, Huang H, Bashir K, Li C. Isolated Sn on mesoporous silica as a highly stable and selective catalyst for the propane dehydrogenation. *Appl Catal A Gen* 2020;590:117291. DOI

58. Salmones J, Wang J, Galicia JA, Aguilar-rios G. H_2 reduction behaviors and catalytic performance of bimetallic tin-modified platinum catalysts for propane dehydrogenation. *J Mol Catal A Chem* 2002;184:203-13. DOI

59. Petit C, Rehspringer JL, Kaddouri A, Libs S, Poix P, Kiennemann A. Oxidative coupling of methane by pyrochlore oxide $A_2B_2O_7$ (A = rare earth, B = Ti, Zr, Sn). Relation between C_2 selectivity and B-O bond energy. *Catal Today* 1992;13:409-16. DOI

60. Zhang C, Liu X, Jiang M, Wen Y, Zhang J, Qian G. A review on identification, quantification, and transformation of active species in SCR by EPR spectroscopy. *Environ Sci Pollut Res Int* 2023;30:28550-62. DOI

61. Shi Y, Wang X, Chen L, et al. In situ DRIFT study on NH_3 selective catalytic reduction of NO_x over HBEA zeolite doped with CeO_2. *Appl Surf Sci* 2020;506:144715. DOI

62. Choudhary V. Acidity/basicity of rare-earth oxides and their catalytic activity in oxidative coupling of methane to C_2-hydrocarbons. *J Catal* 1991;130:411-22. DOI

63. Scott JF, Palai R, Kumar A, et al. New phase transitions in perovskite oxides: $BiFeO_3$, $SrSnO_3$, and $Pb(Fe_{2/3}W_{1/3})_{1/2}Ti_{1/2}O_3$. *J Am Ceram Soc* 2008;91:1762-8. DOI

Rumeng Ouyang

Rumeng Ouyang graduated with a B.S. in 2022 from the School of Chemistry and Chemical Engineering of Gannan Normal University. She is now pursuing a Master's degree at Nanchang University under the supervision of Professor Xiang Wang. Her research focuses on catalytic methane oxidative coupling.

Junwei Xu

Dr. Junwei Xu received his Ph.D. in 2019 from the School of Chemistry and Chemical Engineering at Nanchang University under the supervision of Professor Xiang Wang. He completed his postdoctoral research at Nanchang University in 2022 and is currently an associate professor at the Institute of Applied Chemistry, Jiangxi Academy of Sciences. With over eight years of experience, he has specialized in the development of pyrochlore catalytic materials for the activation and added value transformation of small molecule alkanes. Dr. Xu has published around 30 research articles in top-tier journals including *ACS Catalysis*, *Journal of Catalysis* and *Journal of Physical Chemistry Letters*, which collectively have been cited over 300 times.

Xusheng Zhong

Xusheng Zhong received his B.S. degree in 2021 and his Master's degree in June 2024 from the School of Chemistry and Chemical Engineering of Nanchang University under the supervision of Professor Xiang Wang. His research interests revolve around methane oxidative coupling and ethane dehydrogenation to ethylene.

Ying Gong received her B.S. degree in Chemistry and Chemical Engineering from Nanchang Hangkong University in 2020 and completed her Master's degree at Nanchang University in 2023 under the supervision of Professor Xiang Wang. Her research centers on oxidative coupling of methane.

Ying Gong

Yameng Liu received his B.S. degree in 2019 and his Master's degree in 2023 from the School of Chemistry and Chemical Engineering of Nanchang University under the supervision of Professor Xianglan Xu. He is now pursuing his Ph.D. at China University of Petroleum (East China). His current research interests lie in multi-scale material computation.

Yameng Liu

Dr. Xiuzhong Fang received his PhD from the School of Chemistry and Chemical Engineering at Nanchang University in 2016, under the supervision of Professor Xiang Wang. After completing a postdoctoral fellowship at the School of Energy and Environment, Beijing University of Technology, from 2017 to 2019, he returned to Nanchang University as an associate professor. Dr. Fang's research is at the cutting edge of hydrogen production, focusing on low carbon hydrocarbon reforming, methane dry reforming, and catalytic conversion of carbon dioxide.

Xiuzhong Fang

Dr. Jiating Shen received his Ph.D. from Nanchang University in 2019 under the supervision of Professor Xiang Wang. Since 2007, he has been actively engaged in teaching and scientific research at the School of Chemistry and Chemical Engineering at Nanchang University. His research spans a wide range of fields, including physical chemistry, industrial catalysis, heterogeneous catalysis, environmental catalysis and surface chemistry.

Jiating Shen

Professor Xiang Wang received his Ph.D. from the School of Chemistry and Molecular Engineering at Peking University in 1998 under the supervision of Professor Youchang Xie. He then conducted postdoctoral research under the supervision of Professor Wolfgang Sachtler at Northwestern University, Center for Catalysis and Surface Science from 1998 to 2000, followed by research with Professor Raymond Gorte at the University of Pennsylvania, Department of Chemical Engineering from 2000 to 2002. From 2002 to 2005, he worked as a research associate with Professor Israel Wachs at Lehigh University, Department of Chemical Engineering. Following his academic career, Professor Wang joined EverNu Technology LLC in the United States as a Senior Research Scientist (2005-2008) and later worked as a Research Chemist II at BASF Catalysts LLC (2008-2010). Since 2010, he returned to academia as the Ganjiang Distinguished Professor at Nanchang University, where he has since led groundbreaking research in heterogeneous catalysis, industrial catalysis and surface structural chemistry, including the directions of air pollution control, green energy transformation, rare earth catalysis. Professor Wang has published around 300 research articles in leading journals including *ACS Catalysis*, *Journal of Catalysis*, *Chinese Journal of Catalysis*, and *Journal of Physical Chemistry Letters*, with his work collectively cited over 6500 times. Recognized internationally as an expert, he has been invited to deliver lectures at more than 40 symposiums worldwide since 2010.

Xiang Wang